Electronic Supplementary Material (ESI) for ChemComm.

Filling vacancies in a Prussian blue analogue using mechanochemical post-synthetic modification:

SUPPLEMENTARY INFORMATION

John Cattermull,[a] Samuel Wheeler,[b] Kevin Hurlbutt,[b] Mauro Pasta[b] and and Andrew L. Goodwin[a*]

[a]Department of Chemistry, University of Oxford, Inorganic Chemistry Laboratory, South Parks Road, Oxford OX1 3QR, U.K.

[b]Department of Materials, University of Oxford, Parks Road, Oxford OX1 3PH, U.K.

*To whom correspondence should be addressed;

E-mail: andrew.goodwin@chem.ox.ac.uk

Contents

1 PBA synthesis **3**

2 Post-synthetic modification of PBA samples using ball-milling **4**

3 Inductively coupled plasma mass spectrometry (ICP-MS) **5**

4 Powder X-ray diffraction **8**

5 Justification of α parameter **18**

6 Empirical fits **20**

7 Effects of varying hexacyanometallate anion and milling rate **21**

8 References **22**

1 PBA synthesis

All reagents were obtained from commercial suppliers and used as received. A powder sample of $Mn[Co(CN)_6]_{2/3} \cdot xH_2O$ was prepared following the coprecipitation method described in Ref. S 1. An aqueous solution of $MnSO_4{\cdot}H_2O$ (0.75 M) was added dropwise to an equal volume of aqueous $K_3[Co(CN)_6]$ solution (0.75 M) to give a colourless precipitate. The mixture was stirred at room temperature for two hours. The solid was subsequently isolated by vacuum filtration, washed with deionised water, and dried for 24 h in a vacuum oven at 120 °C. The yield obtained was essentially quantitative with respect to the manganese-containing precursor. The phase purity of the product was verified by powder X-ray diffraction (PXRD) and infrared spectroscopy, and the Mn:Co ratio determined using inductively coupled plasma mass spectrometry (ICP-MS) as described below and in the main text.

2 Post-synthetic modification of PBA samples using ball-milling

Powder samples of $Mn[Co(CN)_6]_{2/3} \cdot xH_2O$ (416.2 mg, prepared as described in Section 1) and $K_3[Co(CN)_6]$ (232.5 mg) were mixed finely and added to a stainless steel grinding vessel containing two stainless steel ball bearings (5 mm diameter). On the basis that x is small, these quantities correspond to a 3:1 molar ratio of reagents. The grinding vessel was loaded onto a Retsch MM400 Mixer Mill, and its contents milled neat for up to 180 mins at a rate of 20 Hz.

Separate milling experiments were carried out for subsequent analysis by PXRD, on the one hand, and by ICP-MS, on the other hand. In the former case, trace quantities of Al_2O_3 were added as a PXRD standard. Milling proceeded for a total of 80 mins, with the process paused after periods of $t = 10, 20, 30, 40, 50,$ and 60 mins. At each point a suitable quantity of the mixture was removed for PXRD analysis and then returned post-analysis to the grinding vessel. For the ICP-MS production runs, milling was allowed to continue for 180 mins. A small fraction of the mixed sample ($\sim$15 mg) was removed after milling periods of $t = 5, 10, 20, 30, 40, 60, 90,$ and 120 mins for ICP-MS analysis. Because this analysis is destructive the total quantity of sample diminished during these production runs. With this in mind, the quantity of sample removed was kept as small as practicable so as to minimise any effect on reaction rate arising from changes in mass quantity within the ball mill.

3 Inductively coupled plasma mass spectrometry (ICP-MS)

For each ball-milled sample prepared as described in Section 2, the solid mixture was prepared for ICP-MS analysis as follows. Unreacted $K_3[Co(CN)_6]$ was first removed by washing in triplicate with an excess of deionised water. The insoluble PBA component was isolated by centrifugation, digested in nitric acid, and the resulting solution diluted with deionised water to give a final nitrate concentration of 2% and a Mn concentration of approximately 300 parts per billion (ppb).

Calibration for Mn and Co compositions was achieved through a series of standard nitrate solutions (Certipur, Merck) of known compositions; we used final concentrations of 0, 50, 100, 150, . . ., 500 ppb, giving a total of $22 = 11 \times 2$ standards.

For each of the milled samples and for each standard solution, the corresponding Mn and Co compositions were determined using a Shimadzu ICPMS-2030 spectrometer coupled with a mini torch and an AS-10 autosampler. A helium collision cell was used to remove interfering polyatomic species. Measurements were performed in triplicate, with washing runs carried out between successive measurements. The measured ICP-MS intensities I(Co), I(Mn) for our series of standard solutions are listed in Table S1 as a function of nominal compositions $f_{\rm nom}$(Co), $f_{\rm nom}$(Mn). From these data we determined the following calibration relations:

$$f(\mathrm{Co})/\mathrm{ppb} = -1.8(11) + 0.3231(12) \times I(\mathrm{Co})/\mathrm{cps}, \quad (1)$$

$$f(\mathrm{Mn})/\mathrm{ppb} = -4(5) + 1.94(3) \times I(\mathrm{Mn})/\mathrm{cps}. \quad (2)$$

The ICP-MS intensities for our milled samples and the corresponding Co, Mn compositions, determined using Eqs. (1) and (2), are listed in Table S2. Given also are the corresponding Co/Mn ratios ϕ, which in turn are reported in Fig. 2(a) of the main text.

f_{nom}(Co)/ppb	f_{nom}(Mn)/ppb	I(Co)/cps	I(Mn)/cps
0	0	0.0790(15)	0.020(3)
50	0	167.06(13)	0.739(11)
100	0	324.8(16)	0.320(3)
150	0	461.8(18)	0.545(9)
200	0	616.4(19)	0.441(2)
250	0	773(3)	0.695(6)
300	0	941(3)	1.230(17)
350	0	1096(5)	0.887(10)
400	0	1254(5)	0.437(13)
450	0	1398(8)	2.00(3)
500	0	1543(11)	1.412(3)
0	0	0.102(5)	0.0223(17)
0	50	2.77(4)	28.38(17)
0	100	2.85(3)	51.99(18)
0	150	2.20(4)	81.96(13)
0	200	2.668(14)	111.39(13)
0	250	3.01(4)	137.3(4)
0	300	2.667(14)	167.2(4)
0	350	2.78(2)	163.3(17)
0	400	2.575(5)	198.3(19)
0	450	3.024(19)	233.4(12)
0	500	2.70(3)	264.9(6)

Table S1: Raw ICP-MS data used to construct calibration curves for Co and Mn compositions.

t/min	I(Co)/cps	I(Mn)/cps	f(Co)/ppb	f(Mn)/ppb	ϕ
0	828(4)	197.4(12)	266(2)	379(9)	0.700(17)
5	721(3)	166.30(15)	231.0(17)	319(8)	0.724(19)
10	729(3)	165.3(10)	233.4(17)	317(8)	0.736(19)
20	719.3(18)	158.4(3)	230.6(15)	304(8)	0.76(2)
30	577(3)	128.5(6)	184.5(13)	246(7)	0.75(2)
40	587.8(16)	131.5(4)	188.1(14)	252(7)	0.75(2)
60	583(3)	126.8(3)	186.6(16)	242(7)	0.77(2)
90	575(2)	122.0(8)	183.8(15)	233(7)	0.79(2)
120	457.2(11)	96.9(8)	145.9(13)	184(6)	0.79(3)
180	546(2)	114.0(2)	174.5(15)	218(7)	0.80(3)

Table S2: Measured ICP-MS data for milled PBA samples, derived Co and Mn concentrations f, and corresponding Co:Mn ratios ϕ.

4 Powder X-ray diffraction

Methodology

Powder X-ray diffraction measurements were carried out using a Bruker D8 Advance Eco Diffractometer operated in flat-plate geometry with CuKα radiation. Each measurement consisted of a 20-minute scan over the angular range $2\theta = 7$–90°. Alumina was used as internal standard; all measurements were carried out at ambient temperature and pressure.

Our refinement strategy consisted of two stages. The goal of the first stage was to determine the relative phase fractions of PBA and $K_3[Co(CN)_6]$ as a function of milling time; *i.e.* to determine the function $f_{\mathrm{K}}(t)$ as shown in the left-hand panel of Fig. 2(c) of the main text. To do so, we employed a mixed Pawley/Rietveld approach implemented in TOPAS Academic (version 6).[S3] Both the Al_2O_3 standard ($R\bar{3}c$, $a \sim 4.8\,$Å, $c \sim 13.0\,$Å) and the $K_3[Co(CN)_6]$ phase ($P2_1/c$, $a \sim 7.0\,$Å, $b \sim 10.4\,$Å, $c \sim 8.4\,$Å, $\beta \sim 108^\circ$)[S4] were included explicitly; unit-cell dimensions, atomic displacement parameters, phase fractions, a modified Thompson-Cox-Hasting pseudo-Voigt (TCHZ) peak shape function and a simple axial divergence correction were included as refineable parameters (but not the atomic positions within either the $K_3[Co(CN)_6]$ or Al_2O_3 phases). At the same time, the PBA component ($Fm\bar{3}m$, $a \sim 10.4\,$Å) was accounted for by a Pawley refinement.[S2] Our reasoning for doing so was that we did not want to presume a specific composition and hydration structural model. Intensities were allowed to refine for the unmilled ($t = 0$) data set, and these were then fixed in subsequent refinements of $t > 0$ data within this first analysis stage, with only the overall phase scale factor, peak shape, and unit-cell dimensions allowed to refine. The PBA scale factors so obtained are the values $f_{\mathrm{PBA}}(t)$ used in Eq. (2) of the main text.

The reflection intensities of the $K_3[Co(CN)_6]$ phase showed evidence of strong preferred orientation effects for milled samples ($t > 0$). Consequently we included a fourth-order spherical harmonics preferred orientation correction for this phase. The corresponding crystallite orientation tensor corresponded to preferred orientation along the stacking axis of the layered $K_3[Co(CN)_6]$ structure, which is sensible in a flat-plate geometry such as we used here. As an additional check of this interpretation, we carried out a further set of milling experiments under identical conditions but including *only* $K_3[Co(CN)_6]$, and observed the same qualitative changes in diffraction pattern. Preferred orientation effects are responsible for the ostensible variability in reduction of different $K_3[Co(CN)_6]$ reflection intensities with milling time; for example, the reflection at $2\theta \sim 22^\circ$ decreases with milling more slowly than that at 13°

[Fig. 2(b) of the main text].

In the second stage of our PXRD refinement strategy, we fixed the PBA phase fractions as determined in the first stage, and subsequently allowed the reflection intensities of this PBA phase to refine. This allowed us to determine the changes in (200) and (400) reflection intensities used to derive the variation in α with t as shown in the right-hand panel of Fig. 2(c) of the main text.

Refinement results

The key results of our refinements are summarised in Table S3, and the corresponding fits to data are shown in Figs. S1–S8. In addition to the preferred orientation effects discussed above, we found an increase in the peak widths associated with both $K_3[Co(CN)_6]$ and PBA phases with increasing milling time, which we associate with a decrease in crystallite size.

t/min	f_{PBA}	x_{K}	$I(400)$	$I(200)$	a_{PBA}/Å	f_{K}	α	Δm_{rel}/%
0	1	1.000(12)	38.2(6)	8.04(10)	10.4369(3)	1.000(12)	2.18(5)	0.0
10	0.962(7)	0.832(9)	36.6(5)	7.54(8)	10.4420(2)	0.865(10)	2.20(4)	9.1(16)
20	1.016(7)	0.694(9)	39.7(5)	7.88(8)	10.4395(3)	0.683(11)	2.25(4)	22.9(15)
30	0.984(8)	0.647(10)	40.7(5)	7.64(8)	10.4417(4)	0.657(11)	2.31(4)	25.1(16)
40	0.999(8)	0.625(11)	41.8(5)	7.52(8)	10.4428(4)	0.626(12)	2.36(4)	27.7(16)
50	1.053(10)	0.612(13)	44.1(6)	7.67(8)	10.4440(5)	0.581(16)	2.40(4)	31.6(18)
60	1.130(10)	0.654(13)	45.6(6)	8.31(8)	10.4417(5)	0.58(2)	2.34(4)	31.8(17)
80	1.160(10)	0.595(14)	46.3(6)	8.72(8)	10.4458(5)	0.51(2)	2.30(4)	37.8(17)

Table S3: Key refinement parameters determined by joint Rietveld/Pawley refinement of our PXRD data. The final parameter Δm_{rel} is the Rietveld-refined relative mass loss of $K_3[Co(CN)_6]$.

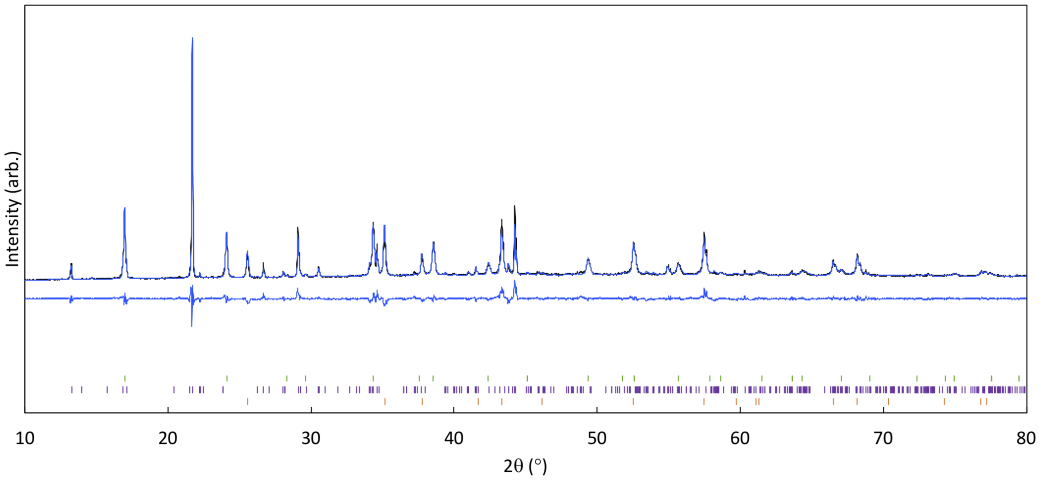

Figure S1: Powder X-ray diffraction pattern for the unmilled reaction mixture (black line; CuKα radiation), and fit (blue red curve, respectively) as described in the text. Note that for this initial data set the fits obtained in both stages 1 and 2 are identical. The corresponding difference curve (data $-$ fit) is offset below the data. Tick marks denote reflection positions for the PBA (green), $K_3[Co(CN)_6]$ (purple), and Al_2O_3 (orange) phases.

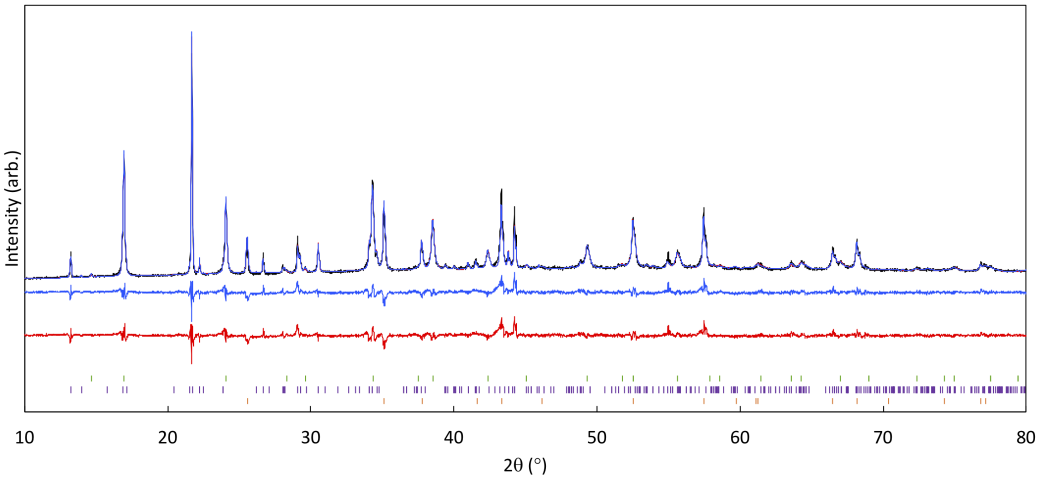

Figure S2: Powder X-ray diffraction pattern for the reaction mixture milled for 10 mins (black line; CuKα radiation), and stage-1/stage-2 fits (blue and red curves, respectively) as described in the text. Difference curves (data $-$ fit) are offset below the data, coloured as for the corresponding fits. Tick marks denote reflection positions for the PBA (green), $K_3[Co(CN)_6]$ (purple), and Al_2O_3 (orange) phases.

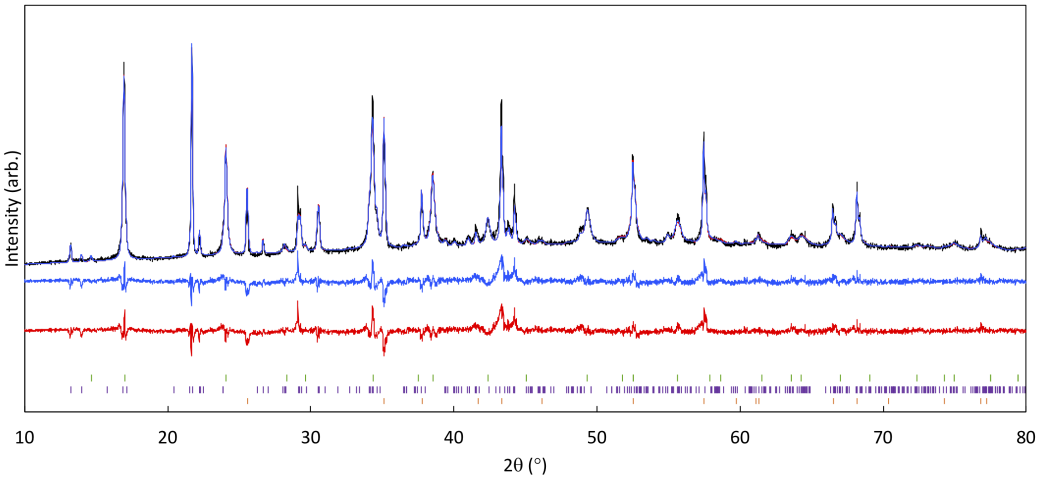

Figure S3: Powder X-ray diffraction pattern for the reaction mixture milled for 20 mins (black line; CuKα radiation), and stage-1/stage-2 fits (blue and red curves, respectively) as described in the text. Difference curves (data $-$ fit) are offset below the data, coloured as for the corresponding fits. Tick marks denote reflection positions for the PBA (green), $K_3[Co(CN)_6]$ (purple), and Al_2O_3 (orange) phases.

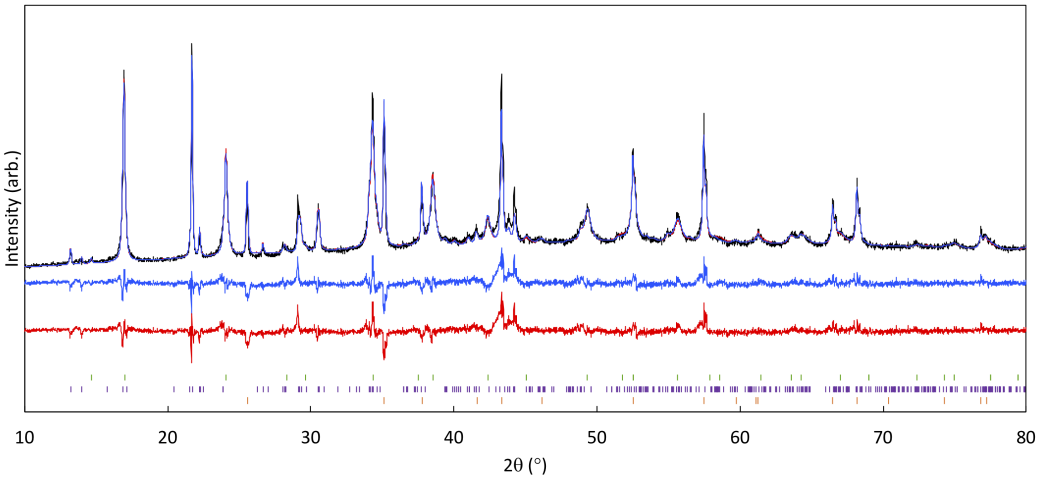

Figure S4: Powder X-ray diffraction pattern for the reaction mixture milled for 30 mins (black line; CuKα radiation), and stage-1/stage-2 fits (blue and red curves, respectively) as described in the text. Difference curves (data $-$ fit) are offset below the data, coloured as for the corresponding fits. Tick marks denote reflection positions for the PBA (green), $K_3[Co(CN)_6]$ (purple), and Al_2O_3 (orange) phases.

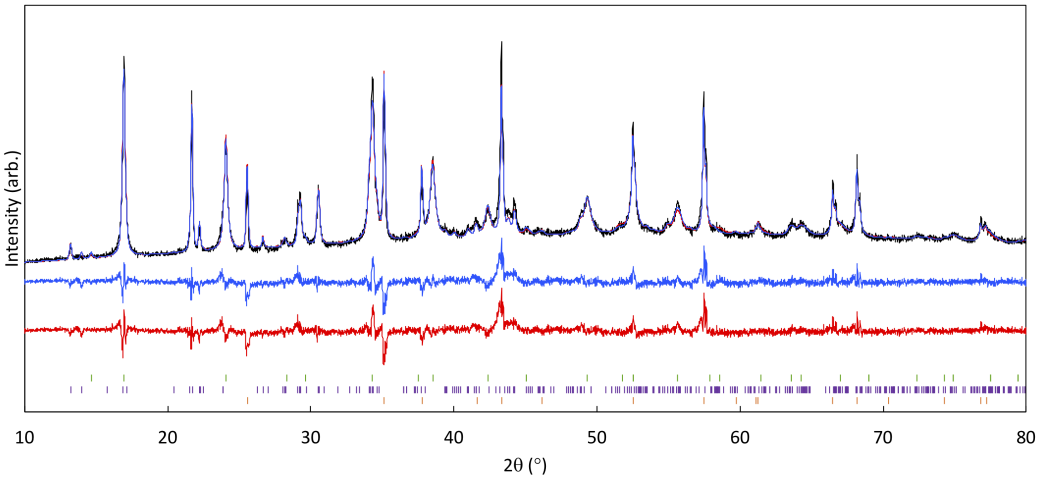

Figure S5: Powder X-ray diffraction pattern for the reaction mixture milled for 40 mins (black line; CuKα radiation), and stage-1/stage-2 fits (blue and red curves, respectively) as described in the text. Difference curves (data $-$ fit) are offset below the data, coloured as for the corresponding fits. Tick marks denote reflection positions for the PBA (green), $K_3[Co(CN)_6]$ (purple), and Al_2O_3 (orange) phases.

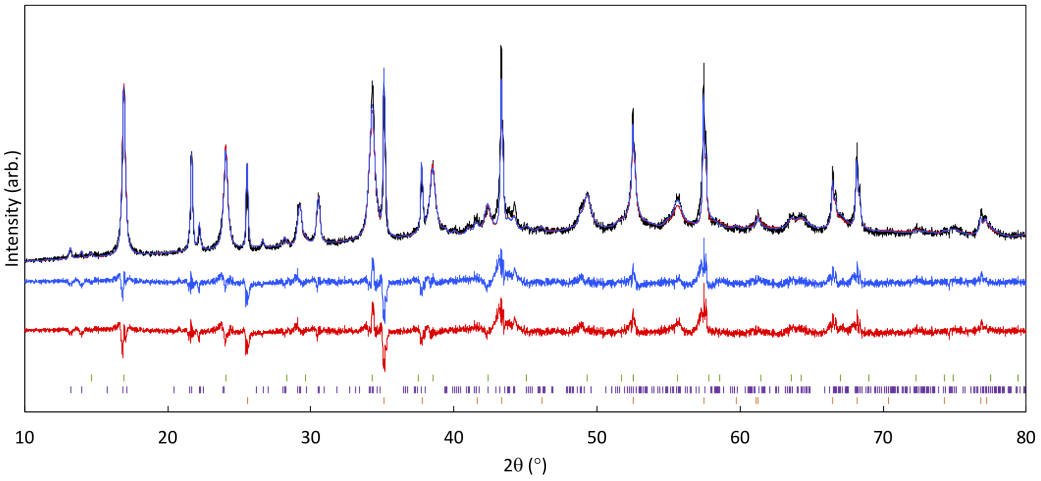

Figure S6: Powder X-ray diffraction pattern for the reaction mixture milled for 50 mins (black line; CuKα radiation), and stage-1/stage-2 fits (blue and red curves, respectively) as described in the text. Difference curves (data $-$ fit) are offset below the data, coloured as for the corresponding fits. Tick marks denote reflection positions for the PBA (green), $K_3[Co(CN)_6]$ (purple), and Al_2O_3 (orange) phases.

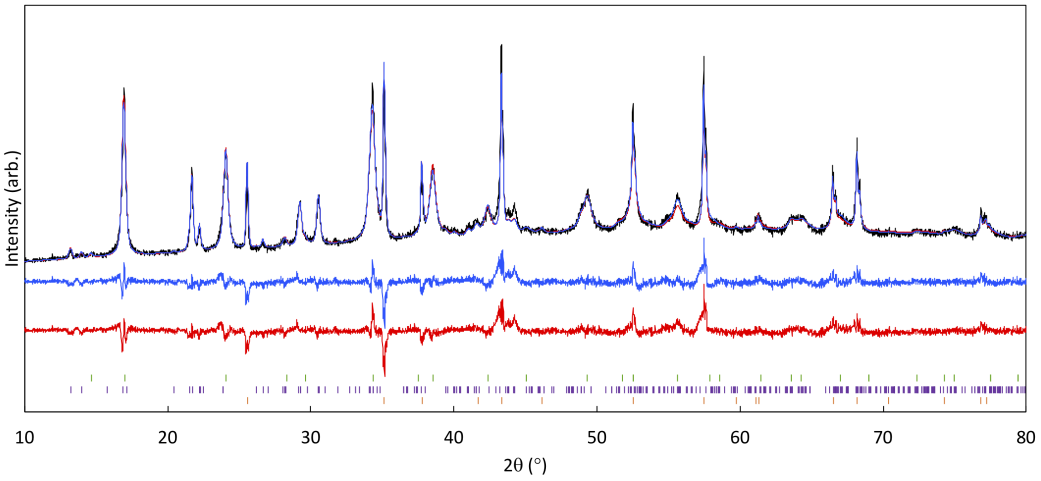

Figure S7: Powder X-ray diffraction pattern for the reaction mixture milled for 60 mins (black line; CuKα radiation), and stage-1/stage-2 fits (blue and red curves, respectively) as described in the text. Difference curves (data $-$ fit) are offset below the data, coloured as for the corresponding fits. Tick marks denote reflection positions for the PBA (green), $K_3[Co(CN)_6]$ (purple), and Al_2O_3 (orange) phases.

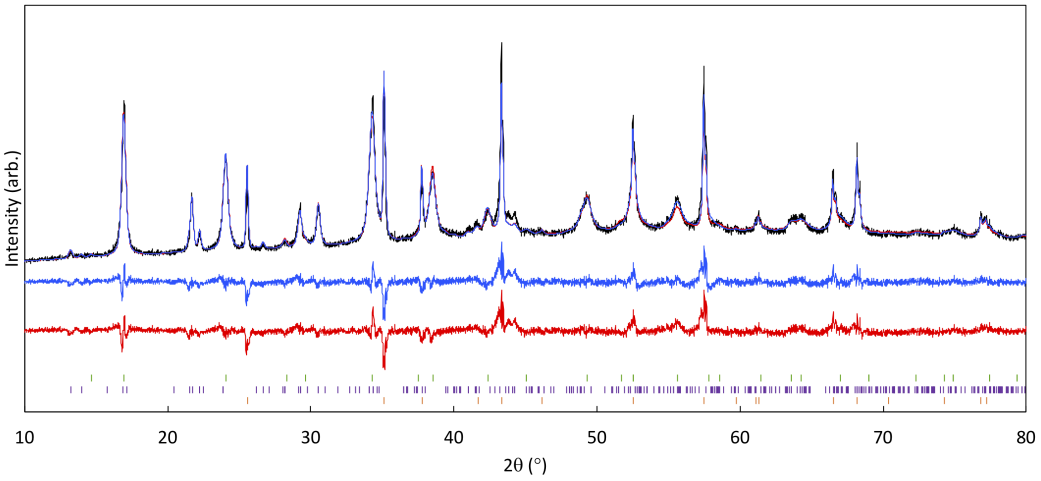

Figure S8: Powder X-ray diffraction pattern for the reaction mixture milled for 80 mins (black line; CuKα radiation), and stage-1/stage-2 fits (blue and red curves, respectively) as described in the text. Difference curves (data $-$ fit) are offset below the data, coloured as for the corresponding fits. Tick marks denote reflection positions for the PBA (green), $K_3[Co(CN)_6]$ (purple), and Al_2O_3 (orange) phases.

5 Justification of α parameter

The generalised crystal structure for dehydrated PBAs has symmetry $Fm\bar{3}m$ and positional parameters / occupancies as given in Table S4.[S2] Here we take the parameter x to denote the degree of vacancy filling, such that the composition at $x = 0$ is $Mn[Co(CN)_6]_{2/3} \cdot 4H_2O$ and at $x = 1$ is $KMn[Co(CN)_6]$. By construction, all structure factors $F(hkl)$ are a linear function of x. We put

$$F(200)(x) = F'_{(200)} + \lambda x, \tag{3}$$

$$F(400)(x) = F'_{(400)} + \mu x. \tag{4}$$

Note that $|\lambda| \ll |F'_{(200)}|$ and $|\mu| \ll |F'_{(400)}|$ as the perturbation captured by x is small. Then the ratio

$$\begin{aligned} \alpha(x) &= \frac{\sqrt{I(400)(x)}}{\sqrt{I(200)(x)}} \\ &= \left| \frac{F'_{(400)} + \lambda x}{F'_{(200)} + \mu x} \right| \\ &\simeq \frac{1}{|F'_{(200)}|^2} \left| F'_{(400)} F'_{(200)} + (\lambda F'_{(200)} - \mu F'_{(400)}) x \right|. \end{aligned} \tag{5}$$

Consequently, α is a linear function of x and variations in α can be interpreted in terms of variations in vacancy fraction and degree of K^+ intercalation. The severity of the approximation in Eq. (5) at the one-third vacancy filling fraction observed experimentally is about 3.5%, when calculated using the structural model given in Table S4.

Atom	Occupancy	Position
Co	$(2+x)/3$	$(0, 0, 0)$
Mn	1	$(\frac{1}{2}, 0, 0)$
C	$(2+x)/3$	$(0.179, 0, 0)$
N	$(2+x)/3$	$(0.288, 0, 0)$
O	$(1-x)/3$	$(0.277, 0, 0)$
K	$x/2$	$(\frac{1}{4}, \frac{1}{4}, \frac{1}{4})$

Table S4: Crystallographic model for a generalised manganese hexacyanocobaltate PBA structure of varying vacancy content, based on that reported in Ref. S2.

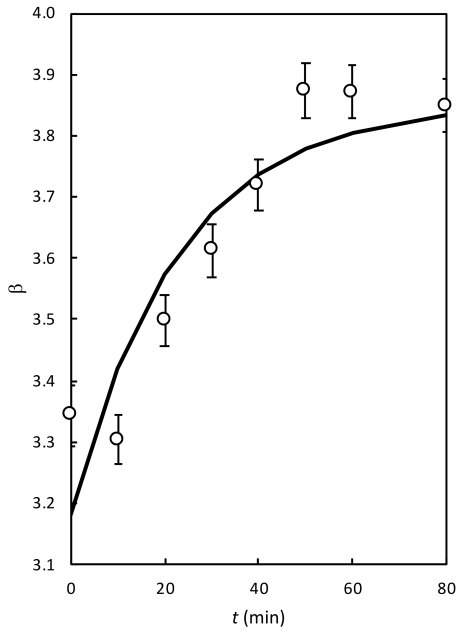

Figure S9: Variation in intensity parameter β with milling time. The solid line shows the corresponding exponential fit $\beta(t) = \beta_\infty + [\beta_0 - \beta_\infty]\exp(-t/\tau)$, where τ is constrained to have the same value as that used in the main text.

Note that while, in principle, any linear combination of $F(200)(x)$ and $F(400)(x)$ is itself a linear function of x, such combinations are more strongly susceptible to variations in absorption, polarisation, and preferred orientation from measurement to measurement. Nevertheless we note for completeness that essentially equivalent behaviour to that shown in Fig. 2(c) of the main text is observed using, for example, the function $\beta = \sqrt{I(400)} - \sqrt{I(200)}$ [Fig. S9].

As a final point we note that the intensities of $(h00)$ reflections are insensitive to the description of K^+ intercalation in terms of occupation of alternate pores ($F\bar{4}3m$ symmetry) or random occupation ($Fm\bar{3}m$ symmetry).

6 Empirical fits

Various quantities extracted from our ICP-MS and PXRD measurements were fitted using the common functional form

$$\gamma(t) = \gamma_\infty + [\gamma_0 - \gamma_\infty] \exp(-t/\tau). \tag{6}$$

Here, γ is a generic variable, γ_0 its limiting value as $t \to 0$, γ_∞ its limiting value as $t \to \infty$, and τ a characteristic decay timescale. This particular function was chosen because it captured the basic trends observed with as few parameters as possible. The parameters obtained in a linear least squares fit to our data are given in Table S5; these were used to generate the solid lines shown in Fig.2(a),(c) of the main text and Fig. S9 of the SI.

γ	γ_0	γ_∞	τ/min
ϕ	0.7101	0.7979	43.16
ϕ	0.7032	0.7837	22.76
f_K	1.009	0.5260	(22.76)
α	2.155	2.358	(22.76)
β	3.178	3.854	(22.76)

Table S5: Fitted parameters for the various observables reported in the main text ($\phi, f_\mathrm{K}, \alpha$) and in the SI ($\beta$). In the top row are the parameters obtained when fitting only to the observed ϕ values; in subsequent rows are the parameters obtained for a global fit with common τ.

7 Effects of varying hexacyanometallate anion and milling rate

In a set of preliminary additional experiments we sought to establish qualitatively the effects of varying (i) the hexacyanometallate anion and (ii) the milling rate. With respect to the former, we observed relatively little influence on the limiting degree of $[M(CN)_6]^{3-}$ incorporation on replacing M = Co by M = Fe whilst maintaining a milling rate of 20 Hz [Fig. S10]. We have access only to pre-milled ($t = 0$ min) and $t = 120$ min samples, so the curve fit we show assumes the same value of τ as determined for M = Co. On subsequently reducing the milling rate by a factor of two, we find a substantial decrease in the limiting degree of $[M(CN)_6]^{3-}$ incorporation, with the limiting remaining fraction $f_{K,\infty}$ of $K_3[M(CN)_6]$ now increased from 0.526 to 0.700. Hence we anticipate that increasing the milling rate beyond 20 Hz is likely to help vacancy filling.

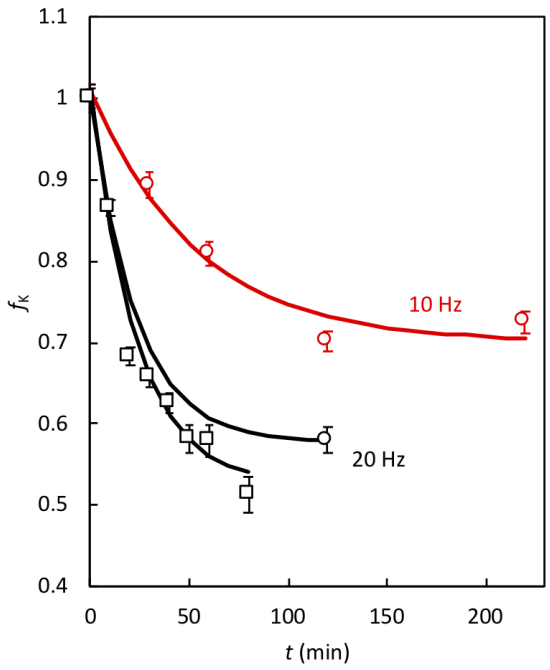

Figure S10: Remaining $K_3[M(CN)_6]$ phase fraction f_K as a function of milling time for M = Co (squares) and Fe (circles) at milling rates of 20 Hz (black symbols) or 10 Hz (red symbols).

8 References

(S1) Simonov, A. *et al.*, *Nature*, **2020**, *578*, 256–260.

(S2) Ludi, A., Güdel, H.-U. and Ruegg, M., *Inorg. Chem.* **1970**, *9*, 2224–2227.

(S3) A. A. Coelho, *TOPAS-Academic, version 6 (computer software)*, Coelho Software, Brisbane.

(S4) Vannerberg, N.-G., *Acta Chem. Scand.* **1972**, *26*, 2863–2876.